Available online at www.sciencedirect.com
ScienceDirect
International Journal of Mass Spectrometry 267 (2007) 159–166
International Journal of Mass Spectrometry
www.elsevier.com/locate/ijms

Modeling ionic unimolecular dissociations from a temperature controlled TPEPICO study on 1-C_4H_9I ions

James P. Kercher[a], Will Stevens[a], Zsolt Gengeliczki[b], Tomas Baer[a,*]

[a] The Department of Chemistry, The University of North Carolina at Chapel Hill, Chapel Hill, NC 27599-3290, United States
[b] Institute of Chemistry, Eötvös Loránd University 1/A Pázmány Péter stny, Budapest 1117, Hungary

Received 13 November 2006; received in revised form 31 January 2007; accepted 20 February 2007
Available online 25 February 2007

Abstract

We report on the development of a new temperature controlled inlet system for the study of gas phase unimolecular reaction dynamics using threshold photoelectron photoion coincidence (TPEPICO) spectroscopy. Temperatures in the range of 220–400 K can be achieved, with a deviation of less than 5 K over the course of a 48 h experiment. Iodine loss from energy selected 1-butyl iodide (1-C_4H_9I) ions was studied at four temperatures, 220, 275, 298 and 400 K. The fractional ion abundances, in the form of breakdown diagrams are presented. Particular attention is paid to the slopes of the molecular and daughter ion abundances in crossover region of the breakdown curve since they are governed solely by the internal energy distribution, $P(E)$, of the neutral precursor. $P(E)$ is a function of both the temperature and vibrational frequencies of the neutral precursor. A detailed discussion regarding the transposition of the neutral thermal energy distribution to the ionic manifold is presented. From the four experimental measurements, the E_0 for the production of the 2-$C_4H_9^+$ ion was determined to be 9.738 ± 0.015 eV.

Keywords: Thermal energy; Butyl iodide; Photoionization; PEPICO; Temperature controlled

1. Introduction

Photoelectron photoion coincidence (PEPICO) spectroscopy is an established tool for the determination of thermochemical properties of gaseous ions, neutrals and radicals [1–14]. PEPICO experiments are most commonly carried out with room temperature samples using a time-of-flight based approach for mass selection. By measuring ions in coincidence with energy selected electrons, the ion internal energy is determined. Time-of-flight (TOF) distributions are collected at several photon energies and the results are easily visualized in the form of a breakdown diagram, which is the fractional abundance of all the ions as a function of the photon energy.

If the dissociation is fast, the 0 K onsets (E_0) can be determined from the disappearance of the parent ion in the breakdown diagram [6,15,16]. Only the internal energy distribution of the neutral precursor is required for modeling the breakdown diagram. Any molecular ions with energy above the dissociation threshold will dissociate immediately and those without sufficient energy remain as parent ions. Integrating over the internal energy distribution, at each photon energy, yields a theoretical breakdown curve to compare with the experimental results. The major assumption in modeling such reactions is that the neutral internal energy distribution is transposed directly to the ion manifold. This assumption has been successfully used in numerous studies, if the temperature was adjusted between 290 and 310 K [17–19]. However, the fit is clearly dependent on the assumed vibrational frequencies so that errors in these values could be compensated for by varying the assumed temperature. The newly developed temperature controlled inlet allows this assumption to be tested at more than one temperature and thus to test this assumption more rigorously.

We have chosen to investigate the 1-butyl iodide molecule with this apparatus because it contains a large number of vibrational modes, particularly in the low frequency region, which contribute significantly to the molecule's thermal energy. A previous PEPICO study [20] on a variety of butyl halides uncovered the role of H-atom transfer in the halogen loss reactions. For example, chlorobutane ions dissociate via HCl loss and the four isomers of bromo and iodobutanes (1-, 2-, *iso*-, and

---

[*] Corresponding author. Tel.: +1 919 962 1580; fax: +1 919 962 2388.
E-mail address: baer@unc.edu (T. Baer).

1387-3806/$ – see front matter © 2007 Elsevier B.V. All rights reserved.
doi:10.1016/j.ijms.2007.02.035

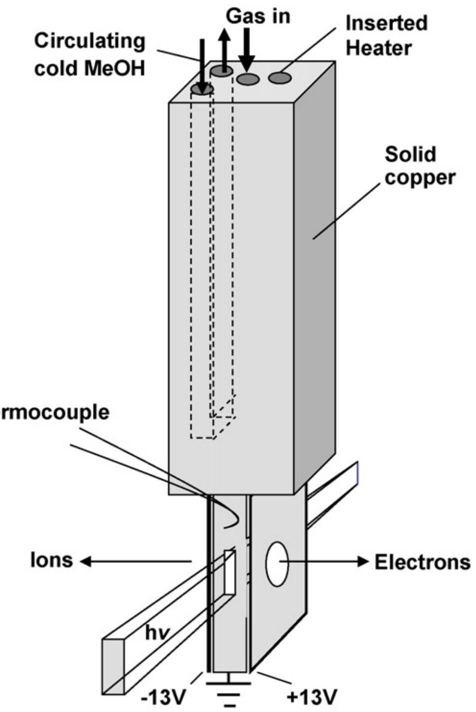

Fig. 1. The temperature controlled cell that is dropped into the ionization region. The solid copper block can be either cooled by circulating cooling fluid, or heated by an inserted heater.

t-) produce only two product $C_4H_9^+$ isomers. The 1- and 2-butylhalides yield the 2-butyl cations (2-$C_4H_9^+$) while the *iso*- and *t*-butylhalides yield the *t*-butyl cation (*t*-$C_4H_9^+$). That is, the loss of I from the 1-butyliodide ion must involve a rearrangement in which an H atom is transferred to generate the 2-$C_4H_9^+$ ion.

2. Experimental approach

The TPEPICO apparatus has been described in detail in previous publications [18,21,22], therefore, we will focus our attention on the implementation of the temperature controlled inlet system. The temperature controlled inlet, shown in Fig. 1, is a 1.5 in. × 1.5 in. × 5 in. solid copper block housing which contains a sample line, cooling line and cartridge heater. The sample line is a 1/4 in. OD copper tube which runs through the center of the block and terminates 2 cm above the VUV light in the center of the ionization region. The tip of the sample line has been flattened to maximize the overlap between the sample vapor and the VUV light. The extraction plates for the ions and electrons are located approximately 6 mm from the ionization spot. They consist of 0.030 in. copper discs with a central hole 0.5 in. in diameter. These plates are in thermal contact with the copper block so that the entire ionization region is isothermal, but are electrically isolated by 0.002 in. Teflon sheets. Cooling is accomplished by flowing ethylene glycol or methanol from a circulating Fisher Isotemp bath (model number 9510) through the copper block cooling line. The bath temperature is digitally controlled, with a range from −30 to +30 °C. In order to optimize the cooling, the length of the cooling lines was minimized, which in turn minimizes temperature fluctuation. Heating is accomplished by using a cartridge heater. Temperatures in the range of 270–400 K can be achieved using the Isotemp bath or the heater. Temperatures, lower than 270 K, were achieved by flowing the ethylene glycol or methanol through a copper coil in an acetone/dry ice bath. The temperature could not be controlled with the Isotemp bath, rather it was monitored and controlled by a hands on approach. In all cases, the temperature was monitored with K type thermocouples at the inlet and outlet of the cooling line as well as directly above the ionization region. The recorded temperature drift is <5 °C over the course of an experiment.

After passing through the inlet, the sample vapor is introduced into the ionization region and ionized with vacuum ultraviolet (VUV) light (tunable from 7 to 14 eV) from a hydrogen discharge lamp dispersed by a 1 m normal incidence monochromator with a resolution of 9 meV at a photon energy of 10.0 eV. The VUV wavelengths are calibrated by using the Lyman-α emission at 1215.67 Å, which is the most intense line in the hydrogen lamp spectrum. The ions and electrons are extracted in opposite directions with an electric field of 20 V/cm. Electrons pass through a second acceleration region where they reach a final energy of 74 eV in the 13 cm long drift region. The applied voltages are designed to velocity focus threshold electrons onto a 1.4 mm aperture at the end of the electron drift region, where a Channeltron detects them. At the same time, energetic electrons focused to concentric rings around the central hole are collected by a second Channeltron after they pass through a 3 mm × 5 mm opening located close to the central 1.4 mm hole. This provides a measure of the hot electron signal which contaminates the threshold.

Ions are accelerated to 100 eV in the first 5 cm long acceleration region and to 280 eV in a short second acceleration region

Table 1
Harmonic vibrational frequencies calculated at the B3LYP/6-311+G* level of theory for relevant species

Species	Frequencies
n-C_4H_9I	84.2[a], 104.6[a], 125.9[a], 225.8, 236.3, 379.4, 578.8, 746.8, 782.0, 904.5, 913.2, 1033.8, 1056.2, 1077.1, 1120.5, 1236.2, 1237.6, 1305.2, 1326.6, 1334.9, 1383.1, 1436.7, 1491.7, 1516.3, 1520.4, 1521.0, 1532.4,3031.5, 3035.7, 3058.2, 3074.1, 3112.9, 3114.2, 127.9, 3129.3, 3195.8
n-$C_4H_9I^+$	79.7, 102.2, 111.5, 198.2, 222.5, 354.8, 477.6, 760.8, 768.6, 802.3, 928.6, 938.7, 989.5, 1016.8, 1048.3, 1190.0, 1248.0, 1249.2, 1275.2, 1282.0, 1310.9, 1406.8, 1442.5, 1466.7, 1506.7, 1512.1, 1521.0, 3007.8, 3069.9, 3088.3, 3111.6, 3126.6, 3144.3, 3155.1, 3171.4, 3250.0
TS[*n*-$C_4H_9\cdots I]^+$	102.2[b], 111.5[b], 198.2, 222.5, 354.8, 477.6, 760.8, 768.6, 802.3, 928.6, 938.7, 989.5, 1016.8, 1048.3, 1190.0, 1248.0, 1249.2, 1275.2, 1282.0, 1310.9, 1406.8, 1442.5, 1466.7, 1506.7, 1512.1, 1521.0, 3007.8, 3069.9, 3088.3,3111.6, 3126.6, 3144.3, 3155.1, 3171.4, 3250.0

[a] Neutral frequencies scaled in 275 K simulations.

[b] Frequencies scaled in modeling asymmetric TOF profiles at 298 K.

after which they travel 48 cm in the drift region before being collected by a tandem multichannel plate ion detector.

3. Calculation of vibrational frequencies

The data analysis, including RRKM rate constant calculations, requires knowledge of the vibrational frequencies of the starting molecule, the molecular ion, as well as the transition state. The calculations on these three species were carried out using the Gaussian 03 program suite [23] provided by the ITS Research computing facility at the University of North Carolina at Chapel Hill. The geometry and vibrational frequencies of all molecules studied were calculated using the Becke 3-parameter exchange functional [24], the electron correlation functional of Lee–Yang–Parr (B3LYP) [25] with the 6-311+G* basis set and are listed in Table 1. No scale factor was applied to the vibrational frequencies of the stable species. The transition states were determined by the QST3 method, using the same level of theory and basis set. This provides a starting set of frequencies for modeling the data. The two lowest frequencies in the transition state are treated as adjustable parameters, as described below.

4. Experimental results

4.1. Ion time-of-flight (TOF) distributions

Normalized time-of-flight (TOF) distributions at 9.61 eV for the central electron collector at each temperature are given in Fig. 2. These spectra have not been corrected for the hot electron contamination and therefore the parent ion is over-represented as compared to the breakdown diagrams. The 1-$C_4H_9I^+$ parent ion is the symmetric peak centered at 31.3 μs and the $C_4H_9^+$ is the slightly asymmetric peak at 17.2 μs. At 220 K (black), the TOF distribution is dominated by the molecular ion 1-$C_4H_9I^+$. The daughter ion, $C_4H_9^+$ is hardly visible. The $C_4H_9^+$ is more pronounced at 273 K (dark grey) and the asymmetry of the peak is observed, but the TOF distribution is still dominated by 1-$C_4H_9I^+$. By 298 K (grey), the $C_4H_9^+$ intensity is strong and the peak is clearly, although only slightly, asymmetric. The TOF spectrum at 400 K (light grey) shows an equal abundance of both 1-$C_4H_9I^+$ and $C_4H_9^+$.

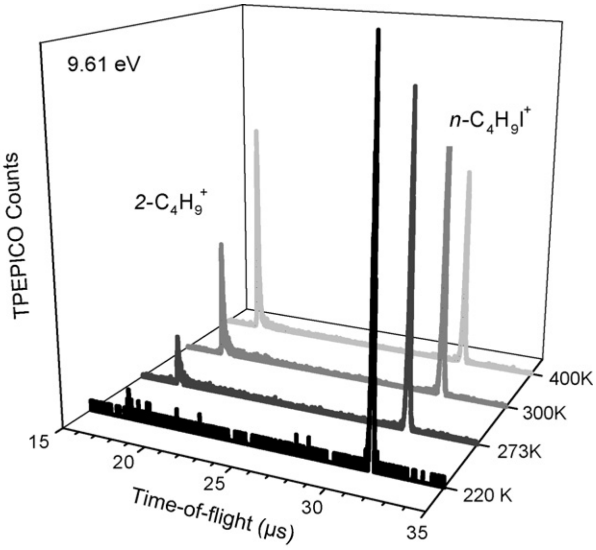

Fig. 2. Normalized time-of-flight distributions at 9.61 eV for the four different temperatures. At 220 K, only the parent ion is observed. As the temperature is increased the thermal energy distribution extends over the dissociation onset and the daughter ion is observed. By 400 K, the two species are equally abundant. These distributions have not been corrected for the hot electron contamination.

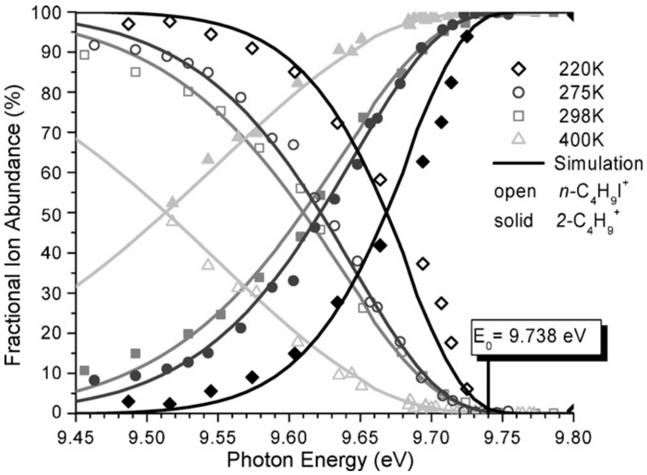

Fig. 3. The breakdown curves at the four temperatures. The open and solid points are the parent and daughter ion fractional abundances, respectively. The solid line is the fit, which results in an E_0 of 9.738 eV.

4.2. Breakdown diagrams

The time-of-flight (TOF) distributions are corrected for the hot electron contamination as previously described [26], and are plotted as breakdown diagrams, which are the fractional abundances of all ions as a function of the photon energy. The experimental breakdown curves from 9.45 to 9.8 eV for the four temperatures are given as the open points for 1-$C_4H_9I^+$ and the solid points for $C_4H_9^+$ in Fig. 3. The solid lines are the simulated ion abundances. At low photon energies, with the exception of the 400 K experiment (triangles), the breakdown curve is predominantly 1-$C_4H_9I^+$. As the photon energy increases, the 1-$C_4H_9I^+$ signal drops to zero as the $C_4H_9^+$ is produced through $I^\bullet$ loss. The slope of the decreasing 1-$C_4H_9I^+$ signal is sharp for the 220 K experiment (diamonds) and becomes more gradual as the temperature is increased to 400 K (squares). Additionally, the crossover points, where the 1-$C_4H_9I^+$ and $C_4H_9^+$ abundances are 50%, shift to lower photon energies as the temperature increases. Although the shapes of all four breakdown curves differ, the 1-$C_4H_9I^+$ signal disappears at the same energy.

5. Modeling results

Fig. 4 shows the procedure for modeling the breakdown diagrams in Fig. 3. The 1-$C_4H_9I^+$ internal energy, is given by the photon energy, $h\nu$, plus the thermal energy, $P(E) \approx \rho(E)\exp(-E/RT)$, where $\rho(E)$ is the rovibrational density of states. The thermal energy, $P(E)$, is calculated using harmonic vibrational frequencies of the neutral molecule and

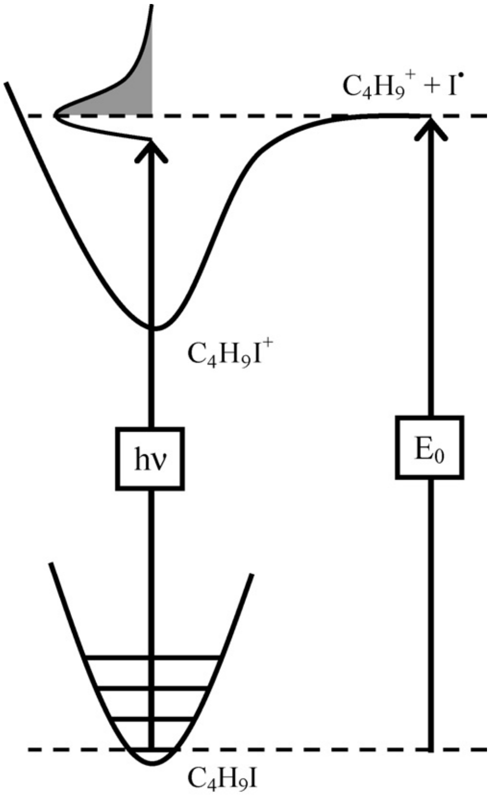

Fig. 4. Diagram showing the production of ions from a neutral sample with a thermal internal energy distribution. It is assumed that all ions with internal energy in excess of the dissociation limit, represented by the grey shaded area, will fragment.

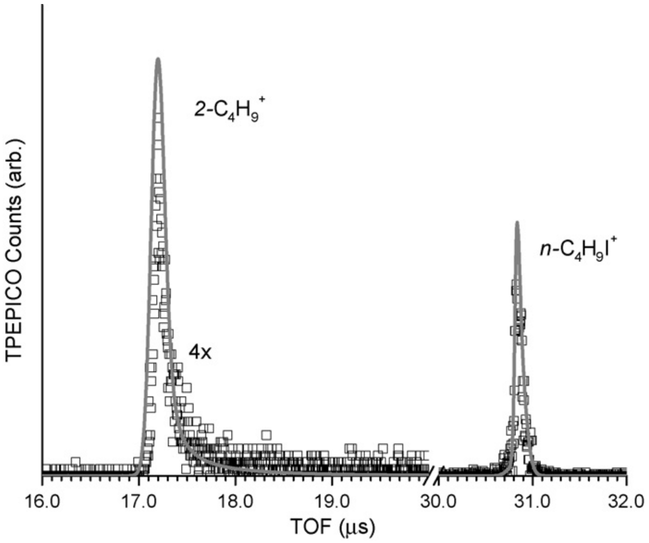

Fig. 5. A time-of-flight distribution at 9.61 eV and 298 K showing the asymmetry of the daughter ion peak. The solid fit reproduces the asymmetry in the daughter ion peak.

the temperature. In addition, we tested the sensitivity to the fit when the three lowest vibrational frequencies were replaced by hindered rotors. As suggested in Fig. 4 for a fast dissociation, all ions with internal energy in excess of the dissociation limit represented by the grey shaded region will generate daughter ions. The breakdown curve can thus be calculated from Eqs. (1) and (2),

$$P(h\nu) = \int_0^{E_0-h\nu} P(E)\,\mathrm{d}E \tag{1}$$

$$D(h\nu) = \int_{E_0-h\nu}^{\infty} P(E)\,\mathrm{d}E \tag{2}$$

where $P(h\nu)$ is the parent ion signal, $D(h\nu)$ the daughter ion signal, E the total energy and E_0 is the dissociation onset. The only adjustable parameter is the E_0.

When modeling the asymmetric TOF profiles resulting from slow dissociations, absolute rate information is required. In this case, the TPEPICO data are modeled within the RRKM framework using the well known equation:

$$k(E) = \frac{\sigma N^{\#}(E - E_0)}{h\rho(E)} \tag{3}$$

where h is the Planck's constant, $\rho(E)$ the density of states of the molecular ion for a total energy E, $N^{\#}(E-E_0)$ the sum of states of the transition state at an energy $E-E_0$, and σ is the symmetry number, which is 1 in this case. The RRKM rates are used to account for a kinetic shift associated with slowly dissociating ions. If the ions do not have time to dissociate during mass analysis, they will appear as parent ions. This results in an overrepresentation of parent ion in the breakdown curve, which would lead to a higher E_0. By modeling both the breakdown curve and TOF distributions simultaneously, a unique $k(E)$ curve is obtained and the E_0 can be extrapolated to the dissociation onset. The molecular ion density of states, $\rho(E)$, is easily calculated from the vibrational frequencies using the Beyer–Swinehart exact counting scheme [27]. In order to fit the calculated $k(E)$ curves to the data, the two lowest transition state vibrational frequencies are adjusted, along with the E_0.

5.1. Room temperature (298 K)

As mentioned earlier, the E_0 can be determined from the disappearance of the parent ion if the dissociation is fast. However, the $C_4H_9^+$ TOF distributions in Fig. 2, and a larger version of this in Fig. 5, are slightly asymmetric, indicating a possible kinetic shift. The magnitude of the kinetic shift was taken into account by modeling both the breakdown curve and several TOF distributions simultaneously by optimizing the E_0 and transition state frequencies. The latter parameter is adjusted to fit the asymmetric TOF profiles to obtain a unique $k(E)$ curve. This simulation of the TOF distribution is shown as the solid line going through the experimental points in Fig. 5, and the breakdown curve in Fig. 3. The derived $k(E)$ curve is extrapolated to the E_0, thus accounting for the kinetic shift. This simulation confirmed that the kinetic shift is negligibly small, i.e., less than 1 meV. The derived 0 K dissociation limit, E_0, was 9.740 ± 0.009 eV. This rate analysis also showed that the transition state that fits these TOF distribution is "tight", with an entropy of activation of −34 J/K (evaluated at 600 K). That is, the transition state frequencies needed to be increased considerably, relative to the ion frequencies (see Table 1). This is consistent with a reaction that involves a rearrangement, rather than a simple dissociation reaction.

The room temperature breakdown diagram and the TOF distributions were fitted with the neutral *n*-butyl iodide frequencies listed in Table 1. The only adjusted parameters were the 0 K onset and the transition state vibrational frequencies. The latter had a neglible effect on the breakdown diagram.

5.2. Dry ice and acetone (220 K) results

The breakdown curve at 220 K is given as the diamonds in Fig. 3 and the solid line is the fit. Several temperatures from 210 to 230 K were modeled and the best fit was obtained at 220 K with an E_0 of 9.736 ± 0.017 eV. The much larger error is due to temperature fluctuation during the course of the experiment. As mentioned above, the temperature could not be controlled digitally and thus depended on the acetone/dry ice ratio and the stirring rate. Since the fractional abundances of the ions change depending on the temperature, as evident from Fig. 2, the breakdown curve has more scatter leading to the larger error in the onset determination. Nevertheless, the resulting E_0 agrees to within 4 meV of the room temperature experiment.

5.3. Two Hundred and Seventy-five Kelvin results

The breakdown curve at 275 K is given as the squares in Fig. 3 and the solid line is the fit. The temperature of the Fischer Isotemp bath used for this experiment was held constant at 273 K, though the measured temperature at the inlet was 275 K. Several temperatures from 260 to 280 K were modeled and the best fit was at 275 K with an E_0 of 9.738 ± 0.010 eV. As in the previous simulations in Fig. 3, the neutral *n*-butyl iodide vibrational frequencies listed in Table 1 were used.

We tested the fitting by treating three of the four low frequency modes as hindered rotors. DFT calculated barriers for the C–C bond rotations were used with the Pitzer rotor [28,29]. However, we noted that the fit to the breakdown diagram was not changed significantly when these frequencies are treated as hindered rotors or as low frequency vibrations. To test the effect of the vibrational frequencies on the thermal energy distribution, and thus the breakdown diagram, we varied these same three frequencies by 0%, 10%, 20% and 30%. As shown in Fig. 6, this also had only a minor effect on the *P*(*E*) distribution. The E_0s resulting from these simulations range from 9.738 eV(no scaling) to 9.745 eV (30%). The range of E_0s is within the experimental uncertainty, however there is a noticeable worsening of the fit to the breakdown curve when these frequencies were increased by 30%.

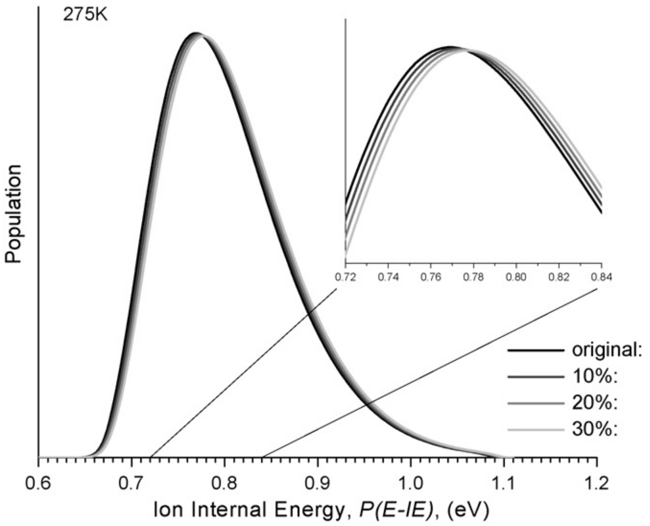

Fig. 6. Four calculated neutral internal energy distributions at 275 K where the lowest four vibrational frequencies were scaled by 0%, 10%, 20%, and 30%. The inset is a blowup of the energy range from 0.72 to 0.84 eV.

5.4. Heated (400 K)

The breakdown curve at a measured temperature of 400 K is given as the triangles in Fig. 3, with the solid line as the fit. Several temperatures from 380 to 410 K were modeled and the best fit was obtained at 400 K (the measured temperature) with an E_0 of 9.738 ± 0.009 eV. The low photon energy data, which correspond to the high energy tail of the thermal energy distribution greatly aid in establishing the best temperature. Because the first experimental point is approximately 50% daughter and parent, the best temperature that fits the data is somewhat more difficult to determine in this data set. Nonetheless, the simulated curve fits very nicely over the entire energy range of the breakdown curve and the determined E_0 agrees very nicely with the three other measurements.

In summary, the breakdown diagrams for all four temperatures were successfully fitted with the unadjusted *n*-butyl iodide vibrational frequencies at temperatures that corresponded within experimental error (±2 K) to the experimentally measured temperatures using the same 0 K dissociation limit.

5.5. Fitting the cross over energies

It was claimed many years ago by us that the 0 K dissociation energy could be determined precisely from the cross over energy at the temperature of the experiment [30]. At the cross over energy, precisely 50% of the ions have sufficient energy

Table 2
Comparison of the cross over energy shift with the average and median thermal energy

Temperature (K)	$C_0 - C_T$ (meV)	Average E_{th} (meV)	Median E_{th} (meV)	ΔC/average E_{th}
220	68	64.5	68	1.054
275	113	98.0	117	1.153
298	125	114	128	1.096
400	223	203	218	1.098

to dissociate. This energy thus corresponds to the median thermal energy of the thermal energy distribution, which is close to the average thermal energy. Because we have established the 0 K onset in this study, we can test how well the cross over energy plus the median thermal energy agrees with this value. Table 2 shows the data for the four temperatures investigated. The agreement between the experimental and calculated cross over energy using the median thermal energy is clearly excellent.

6. Discussion

6.1. The role of thermal energy in ionization

The excellent fit of our calculated breakdown diagrams with calculations based on the neutral thermal energy is rather striking. First of all, it means by measuring the breakdown diagram for a molecule, it is possible to determine directly its internal energy distribution. There is no other experiment that allows one to measure such a distribution for a large polyatomic molecule. Gas phase heat capacities, which can be calculated from the average thermal energy derivative with respect to the temperature, are certainly sensitive to the vibrational modes, but only in an average sense. Similarly, the more easily measured sound velocity depends on the ratio of the heat capacities, $\gamma = C_p/C_v$, which for large molecules approaches 1, and is thus very insensitive to the thermal energy distribution. The use of breakdown diagrams to determine the internal energy distribution may become useful for very large molecules, especially those having long carbon chains, which have many low frequencies that are difficult to calculate by *ab initio* methods.

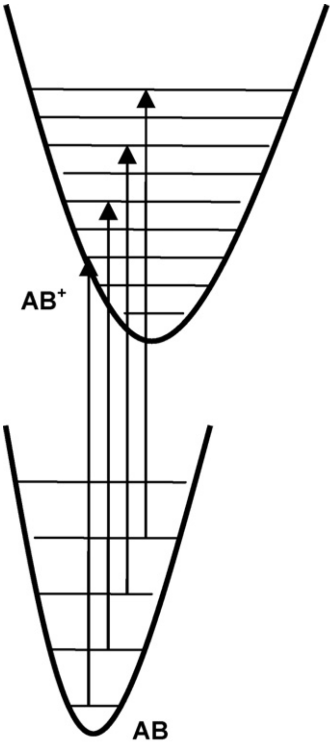

Fig. 7. A series of ionizing transitions of equal photon energies with the neutral and ion frequencies differing by a factor of 2, and the upper state displaced from the lower one by 0.1 Å. The four transitions have Franck–Condon factors as follows: 0–2 (0.068); 1–4 (0.044); 2–6 (0.068); 3–8 (0.055).

We might ask, why the ionization process should simply transpose the thermal energy distribution into the ionic manifold. This is not entirely expected because the distribution of ionic states should depend on Franck–Condon factors, which vary greatly from mode to mode and molecule to molecule. Consider, for instance, a diatomic molecule whose geometries in the neutral and ionic states are identical. If such a molecule is ionized at the ionization energy, we would expect with equal probability, the following transition: $0 \rightarrow 0'$, $1 \rightarrow 1'$, $2 \rightarrow 2'$, etc. where the numbers are the vibrational quantum states in the ground and ionic (primed) states. Under this circumstance, we would expect the thermal energy distribution to be faithfully transposed into the ionic manifold. However, for such a case, all $\mathrm{i} \rightarrow \mathrm{j}'$ transitions would have zero intensities so that the only ion internal energy distributions that could be prepared would be $h\nu + P(E) = IE + P(E)$. That is, photon energies in excess of the ionization energy would simply yield energetic electrons. The same would happen for a polyatomic molecule in which the neutral and ionic geometries are identical. The fact that we can excite ions at any energy, means that removal of the electron changes the geometry and permits preparation of the ion at any photon energy, not just at the ionization energy.

Table 3
n-Butyl iodide frequencies and their contribution to the internal energy at 298 K

Freq-*neutral* (cm^{-1})	E_{ave} (kJ/mol)	E_{total} (kJ/mol)	% of total	Freq-*ion* (cm^{-1})	ΔFrequencies (*neutral* − *ion*)
84.2	166.8	166.8	18.3	79.7	4.5
104.6	158.1	324.9	35.7	102.2	2.4
125.9	149.4	474.3	52.1	111.5	14.4
225.8	113.3	587.6	64.6	198.2	27.6
236.3	109.9	697.6	76.7	222.5	13.8
379.4	71.5	769.1	84.5	354.8	24.6
578.8	37.1	806.1	88.6	477.6	**101.2**
746.8	20.4	826.6	90.8	760.8	−14
782	18.0	844.6	92.8	768.6	13.4
904.5	11.3	856.0	94.1	802.3	**102.2**
913.2	11.0	866.9	95.3	928.6	−15.4

Consider now the situation in which the neutral and ion geometries are very different, as is the case in ammonia. The photoelectron spectrum of NH_3 exhibits a long progression of vibrational peaks in the umbrella mode [31]. Clearly, the Franck–Condon factors favor production of the high v states, which permits photon absorption to produce more highly excited ionic states by $\Delta v > 0$ transitions. Based on simple diatomic displaced harmonic oscillator Franck–Condon factors [32] we note that the transition probabilities for a series of $v' - v = n\,(v = 0, 1, 2, \ldots)$ excitations permits us to excite ions to higher energies. Fig. 7 shows a series of equal photon energy transitions for a diatomic molecule in which the neutral has a frequency of 200 cm^{-1} and the ion 100 cm^{-1}. The Franck–Condon factors, listed in the figure caption, are not equal so that we would not expect that the thermal energy distribution in the neutral state to be faithfully transposed to the ion.

However, in most polyatomic molecules, only a small number of vibrational modes are directly excited. Only those that are symmetric and change significantly from neutral to ion manifold can be excited by $\Delta v = 2, 3, 4$, etc. All other modes follow the $\Delta v = 0$ propensity. In Table 3, we list all the iodobutane frequencies below 1000 cm^{-1}. These are the ones that provide 95% of the 910 cm^{-1} total thermal energy at $T = 298$ K. The last column shows the difference in the ion and neutral frequencies. It is evident, that only two frequencies change significantly ($\Delta \approx 100$ cm^{-1}), and of these only the 578.8 cm^{-1} neutral frequency is significantly populated at room temperature. This mode then provides the ability to excite the ion to high vibrational levels by $\Delta v > 0$ transitions. All the other frequencies will change by the usual $\Delta v = 0$ propensity and thus simply transpose the thermal energy to the ionic manifold without changing it. It is significant that the lowest five frequencies contribute 75% of the thermal energy. It is because of these low frequencies that carry 75% of the thermal energy and are dominated by $\Delta v = 0$ transitions, that we observe a simple transposing of the neutral thermal energy into the ionic manifold.

The above discussion suggests that the larger the molecule, the more likely it is that the sample thermal energy distribution is faithfully transposed to the ionic manifold. It also suggests that this should no longer be the case for smaller molecules, such as CH_3I, where the fraction of vibrational modes that follow $\Delta v = 0$ propensity will be small. We plan on testing this on a series of small and intermediate molecules in a forthcoming study.

6.2. *Reaction mechanism*

The four measured dissociation onsets (average value of 9.738 ± 0.015 eV) for iodine loss agree to within 4 meV. This value is close to a previous PEPICO measurement by Oliveira et al. [20] of 9.720 eV. In that study, the authors pointed out that the 1-butyl iodide ion does not dissociate to the 1-butyl ion, but rather to the lower energy 2-butyl ion, involving an H atom transfer to the terminal carbon atom. This was concluded on the basis of the dissociation onset, which is about 0.7 eV lower than expected for the 1-butyl ion. Our tight transition state is in accord with this.

7. Conclusions

We report here the first results in which a temperature controlled inlet system is used for TPEPICO studies. Temperatures in the range of 220–400 K can be achieved, as illustrated by investigating the iodine loss channel from 1-butyl iodide ions. The breakdown diagrams were fitted by assuming that the neutral thermal energy distribution is transposed into the ionic manifold. The explanation of this interesting fact is based on the fact that in large molecules, most of the Franck–Condon factors connecting the neutral and the ionic states follow the $\Delta v = 0$ propensity, which results in transitions that conserve the thermal energy. This study demonstrates that the thermal energy distribution of polyatomic molecules can be obtained from the breakdown diagrams obtained by PEPICO technique. As far as we know, this is the only experimental method that can derive this information. It may be useful for large molecules with many low frequency modes that are difficult to calculate by *ab initio* methods.

Acknowledgement

We gratefully thank the Department of Energy and the International Office of the National Science Foundation for the support of this work.

References

[1] T. Baer, Int. J. Mass Spectrom. 200 (2000) 443–457.
[2] K. Johnson, I. Powis, C.J. Danby, J. Chem. Phys. 70 (1982) 329–343.
[3] J.P. Gilman, T. Hsieh, G.G. Meisels, J. Chem. Phys. 78 (1983) 3767–3773.
[4] S. Nourbakhsh, K. Norwood, H.M. Yin, C.L. Liao, C.Y. Ng, J. Chem. Phys. 95 (1991) 5014–5023.
[5] J. Mähnert, F. Güthe, K.M. Weitzel, Ber. Bunsen. Phys. Chem. 100 (1996) 1899–1905.
[6] T. Baer, J.A. Booze, K.M. Weitzel, in: C.Y. Ng (Ed.), Vacuum Ultraviolet Photoionization and Photodissociation of Molecules and Clusters, World Scientific, Singapore, 1991, pp. 259–298.
[7] R. Bombach, J. Dannacher, J.P. Stadelmann, J. Am. Chem. Soc. 105 (1983) 1824–1829.
[8] J. Dannacher, Chem. Phys. 29 (1978) 339–344.
[9] Y. Li, B. Sztáray, T. Baer, J. Am. Chem. Soc. 123 (2001) 9388–9396.
[10] P.M. Mayer, T. Baer, Chem. Phys. Lett. 261 (1996) 155–159.
[11] J. Riley, T. Baer, J. Am. Soc. Mass Spectrom. 2 (1991) 464–469.
[12] H.M. Rosenstock, R. Stockbauer, A.C. Parr, J. Chem. Phys. 73 (1980) 773–777.
[13] B. Sztáray, T.J. Baer, Am. Chem. Soc. 122 (2000) 9219–9226.
[14] K.M. Weitzel, J.A. Booze, T. Baer, Int. J. Mass Spectrom. Ion Process. 707 (1991) 301–317.
[15] T. Baer, Int. J. Mass Spectrom. (2000) 204.
[16] T. Baer, B. Sztáray, J.P. Kercher, A.F. Lago, A. Bodi, C. Scull, D. Palathinkal, Phys. Chem. Chem. Phys. 7 (2005) 1507–1513.
[17] A. Bodi, J.P. Kercher, T. Baer, B. Sztáray, J. Phys. Chem. B 109 (2005) 8393–8399.
[18] E.A. Fogleman, H. Koizumi, J.P. Kercher, B. Sztáray, T. Baer, J. Phys. Chem. A 108 (2004) 5288–5294.
[19] A.F. Lago, J.P. Kercher, A. Bodi, B. Sztáray, B.E. Miller, D. Wurzelmann, T. Baer, J. Phys. Chem. A 109 (2005) 1802–1809.
[20] M.C. Oliveira, T. Baer, S. Olesik, M.A Almoster Ferreira, Int. J. Mass Spectrom. Ion Process. 82 (1988) 299–318.
[21] T. Baer, Y. Li, Int. J. Mass Spectrom. 219 (2002) 381–389.

[22] J.P. Kercher, E.A. Fogleman, H. Koizumi, B. Sztáray, T. Baer, J. Phys. Chem. A 109 (2005) 939–946.

[23] M.J. Frisch, G.W. Trucks, H.B. Schlegel, G.E. Scuseria, M.A. Robb, J.R. Cheeseman, J.A. Montgomery, T. Vreven, K.N. Kudin, J.C. Burant, J.M. Millam, S.S. Iyengar, J. Tomasi, V. Barone, B. Mennucci, M. Cossi, G. Scalmani, N. Rega, G.A. Petersson, H. Nakatsuji, M. Hada, M. Ehara, K. Toyota, R. Fukuda, J. Hasegawa, M. Ishida, T. Nakajima, Y. Honda, O. Kitao, H. Nakai, M. Klene, X. Li, J.E. Knox, H.P. Hratchian, J.B. Cross, C. Adamo, J. Jaramillo, R. Gomperts, F. Stratmann, O. Yazyev, A.J. Austin, R. Cammi, C. Pomelli, J.W. Ochterski, P.Y. Ayala, K. Morokuma, G.A. Voth, P. Salvador, J.J. Dannenberg, V.G. Zakrzewski, S. Dapprich, A.D. Daniels, M.C. Strain, Ö. Farkas, D.K. Malick, A.D. Rabuck, K. Raghavachari, J.B. Foresman, J.V. Ortiz, Q. Cui, A.G. Baboul, S. Clifford, J. Cioslowski, B.B. Stefanov, G. Liu, A. Liashenko, P. Piskorz, I. Komáromi, R.L. Martin, D.J. Fox, T. Keith, M.A. Al-Laham, C.Y. Peng, A. Nanayakkara, M. Challacombe, P.M.W. Gill, B. Johnson, W. Chen, M.W. Wong, C. Gonzalez, J.A. Pople, Gaussian 03, Revision C.02, Gaussian Inc., Pittsburgh, PA, 2004 (Ref Type: Computer Program).

[24] A.D. Becke, J. Chem. Phys. 98 (1993) 5648–5652.

[25] C. Lee, W. Yang, R.G. Parr, Phys. Rev. B 37 (1988) 785–789.

[26] B. Sztáray, T. Baer, Rev. Sci. Instrum. 74 (2003) 3763–3768.

[27] T. Beyer, D.R. Swinehart, Commun. ACM 16 (1913) 379.

[28] K.S. Pitzer, W.D. Gwinn, J. Chem. Phys. 10 (1942) 428–440.

[29] T. Baer, W.L. Hase, Unimolecular Reaction Dynamics: Theory and Experiments, Oxford University Press, New York, 1996.

[30] L. Szepes, T. Baer, J. Am. Chem. Soc. 106 (1984) 273–278.

[31] K. Kimura, S. Katsumata, Y. Achiba, T. Yamazaki, S. Iwata, Handbook of He(I) Photoelectron Spectra of Fundamental Organic Molecules, Halsted Press, New York, 1981.

[32] V.L. Stakhursky, T.A. Miler, Proceedings of the 56th Molecular Spectroscopy Symposium, 2006 (Ref Type: Computer Program).